

## Article

# Lab-Scale Permeability Enhancement by Chemical Treatment in Fractured Granite (Cornubian Batholith) for the United Downs Deep Geothermal Power Project, Cornwall (UK)

Katja E. Schulz \*, Kristian Bär \*  and Ingo Sass

Department of Geothermal Science and Technology, Technische Universität Darmstadt, Schnittspahnstraße 9, 64287 Darmstadt, Germany; sass@geo.tu-darmstadt.de

\* Correspondence: kontakt@schulzks.de (K.E.S.); baer@geo.tu-darmstadt.de (K.B.)

**Abstract:** A hydrothermal doublet system was drilled in a fault-related granitic reservoir in Cornwall. It targets the Porthtowan Fault Zone (PTF), which transects the Carnmenellis granite, one of the onshore plutons of the Cornubian Batholith in SW England. At 5058 m depth (TVD, 5275 m MD) up to 190 °C were reached in the dedicated production well. The injection well is aligned vertically above the production well and reaches a depth of 2393 m MD. As part of the design process for potential chemical stimulation of the open-hole sections of the hydrothermal doublet, lab-scale acidification experiments were performed on outcrop analogue samples from the Cornubian Batholith, which include mineralised veins. The experimental setup comprised autoclave experiments on sample powder and plugs, and core flooding tests on sample plugs to investigate to what degree the permeability of natural and artificial (saw-cut) fractures can be enhanced. All samples were petrologically and petrophysically analysed before and after the acidification experiments to track all changes resulting from the acidification. Based on the comparison of the mineralogical composition of the OAS samples with the drill cuttings from the production well, the results can be transferred to the hydrothermally altered zones around the faults and fractures of the PTF. Core Flooding Tests and Autoclave Experiments result in permeability enhancement factors of 4 to >20 and 0.1 to 40, respectively. Mineral reprecipitation can be avoided in the stimulated samples by sufficient post-flushing.

**Keywords:** enhanced geothermal systems (EGS); fractured granite; core flooding experiments; autoclave experiments; Cornubian Batholith



**Citation:** Schulz, K.E.; Bär, K.; Sass, I. Lab-Scale Permeability Enhancement by Chemical Treatment in Fractured Granite (Cornubian Batholith) for the United Downs Deep Geothermal Power Project, Cornwall (UK). *Geosciences* **2022**, *12*, 35. <https://doi.org/10.3390/geosciences12010035>

Academic Editors: Béatrice A. Ledéser, Ronan L. Hébert, Ghislain Trullenque, Albert Genter, Eléonore Dalmais, Jean Hérisson and Jesús Martínez-Frías

Received: 29 September 2021

Accepted: 10 January 2022

Published: 12 January 2022

**Publisher's Note:** MDPI stays neutral with regard to jurisdictional claims in published maps and institutional affiliations.



**Copyright:** © 2022 by the authors. Licensee MDPI, Basel, Switzerland. This article is an open access article distributed under the terms and conditions of the Creative Commons Attribution (CC BY) license (<https://creativecommons.org/licenses/by/4.0/>).

## 1. Introduction

The geothermal doublet at United Downs in Redruth, Cornwall, consists of the production well UD-1 and the injection well UD-2. UD-1 reaches a depth of 5058 m TVD (true vertical depth)/5275 m MD (measured depth), with an approximately 1.2 km long open-hole section, while the injection well UD-2 reaches 2214 m TVD/2393 m MD, with an approximately 550 m long open-hole section. Geothermal Engineering Limited (GEL) plans the establishment of a geothermal power plant with 1 to 3 MW<sub>el</sub> net energy production [1]. The reservoir rock is the fractured Carnmenellis granite, which is one of the onshore plutons comprising the Cornubian Batholith. It is characterised by a strong geothermal anomaly caused by radioactive decay of U, Th and K in the granite [2]. The geological target structure is the Porthtowan fault zone (PTF), which vertically links the two wells [1]. Since a sufficient reservoir temperature of ~190 °C was reached in the production well, the limiting factor for the project is the hydraulic productivity of the reservoir. For this reason, the analysis of permeability enhancement by chemical treatment in the fractured Cornish granite is the prerequisite for an assessment of the potential effectivity of such stimulation in the pilot project United Downs Deep Geothermal Power (UDDGP).

Around fault zones, a complex permeability pattern develops, which is determined by the characteristics of the fracture network. Permeability can vary by up to five orders of magnitude between unaffected granite and fractured and altered granite [3]. Under reservoir conditions, open fractures will be filled with secondary minerals over time if no tectonic reactivation occurs. These (partly) mineralised fractures can be a relevant target for chemical treatment.

Within the scope of the EU-Horizon2020-project Multidisciplinary and multi-context demonstration of EGS exploration and Exploitation Techniques and potentials (MEET), the elaborated results will be applied at transfer sites in similar geological settings within the Variscan basement of Europe.

### Geological Setting

The geology of Cornwall is dominated by the Cornubian Batholith, which intruded into metasediments during the late phase of the Variscan orogeny in the Early Permian period. The metasediments consist in Devonian and Carboniferous passive continental margin successions, locally termed ‘Killas’, which were affected by regional low-grade metamorphism during Variscan shortening in early Carboniferous (prehnite–pumpellyite facies [4]). During the succeeding post-collisional extension 292–270 Ma ago (Early Permian period) the Cornubian Batholith was emplaced in at least two major phases. It is a peraluminous S-type granite. The source rock of the melt is a meta-greywacke [5]. The emplacement occurred mainly along preexisting fault- and weakness zones, possibly including fault zones related to the extensional reactivation of the Rhenohercynian suture [6]. Whereas the rock exposed at the surface was mapped in detail during the intense Cornish mining activity of the last few centuries [7], the composition and fracturation of the granite in the subsurface are the subject of current investigations. Detailed information can be found, e.g., in the work of Beamish and Busby, Shail and Leveridge, Willis-Richards, Edmunds et al., Yeomans et al., and Ghosh [2,6,8–12].

Simons et al. [5] have classified the intrusion stages of the Cornubian Batholith and provide detailed information about the general mineralogical composition, possible accessory minerals and grain size distribution of the respective granite types (Figure 1). The rock samples analysed in the present study were therefore classified according to Simons et al. [5], although the samples are hydrothermally influenced. Information on the mineralogical composition of the relevant samples is provided in Table 1 and Figure 1.

**Table 1.** Origin of the six analysed samples.

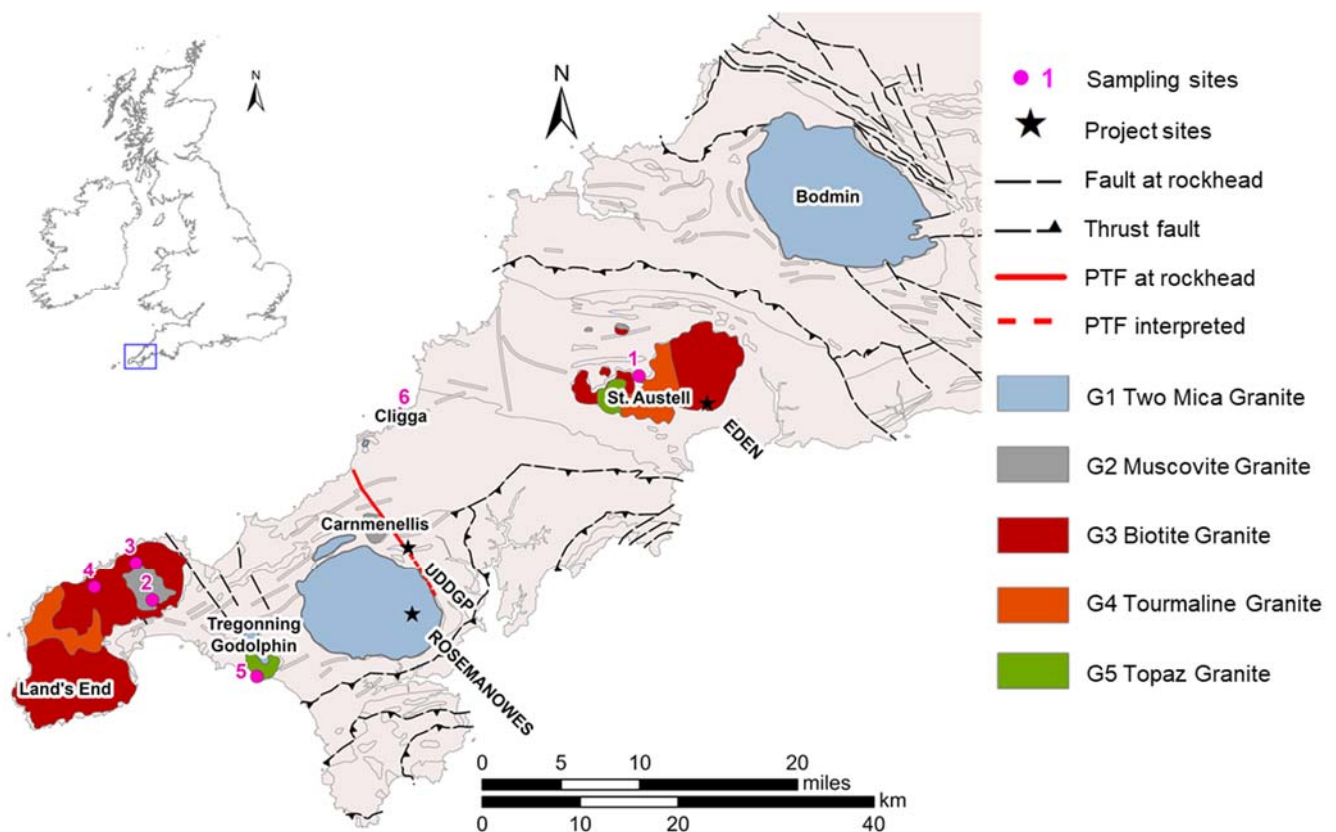
Sample No. (MEETCW)	1 (001004)	2 (010003)	3 (010006)	4 (011003)	5 (017001)	6 (023001)
Granite Complex	St. Austell	Land’s End	Land’s End	Land’s End	Tregonning Godolphin	Cligga
Granite Type, after Simons et al. [5]	G3/G4/G5	G3/G2	G3/G2	G3 (G2)	G5 (G1)	G2
Location Name	IMERYS China clay mining area, Karslake	Castle an Dinas Quarry	Castle an Dinas Quarry	Rosewall Hill	Rinsey Cove	Cligga Head
Location (Brit. Nat. Grid)	SW 98080 57596	SW 48662 34678	SW 48885 34735	SW 46973 38510	SW 59343 26881	SW 73799 53720
Sample Quality, Alteration, Weathering	Fresh quarry sample	Fresh quarry sample	Fresh quarry sample, slightly kaolinised, slightly weathered	Boulders on hill, close to outcrop, partly iron strained	Loose rocks	Loose rocks around abandoned quarry, weathered, greisenisation present in outcrop

Cornwall is intersected by several fault systems, such as the Porthtowan Fault Zone (PTF), which are mainly strike slip faults, roughly trending NW–SE (NNW–SSE) and locally referred to as ‘cross courses’ [9], connecting ENE–WSW-striking extensional faults [13] or dykes, called ‘Elevans’.

The PTF is a NNW–SSE striking strike–slip fault zone (Figure 1). It consists of several fault strands and thus is 200 to 500 m wide at the surface and assumed to be more than 15 km long [1]. The northwestern part was mapped geologically [14] and remotely [11], while the southeastern part is not exposed at the surface and its extent is only presumed from indirect hints (e.g., morphology).

Along the PTF, hydrothermal alteration has affected the mineralogical composition of the reservoir rocks. Two main phases of alteration can be distinguished: younger alteration related to circulation of (partly) meteoric water in structural discontinuities and older alteration related to hydrothermal convection cells around the cooling granitic bodies, with: (a) fluids possibly linked with the first marine incursions in late Triassic and (b) fluids with magmatic origin [4].

Products of hydrothermal alteration are present, such as Kaolinite (likely Dickite at reservoir depth [15–18], greisenisation (paired with tourmalinisation and cassiterite veins [19], Tourmaline veins (related to the circulation of boron-enriched fluids in hydrothermal convection cells [20], Chlorite [20], hydrothermal W/Sn/Cu/As/Zn ore minerals (mainly in the metasediments [4,13] and Quartz, Fluorite or Barite veins [15,21].

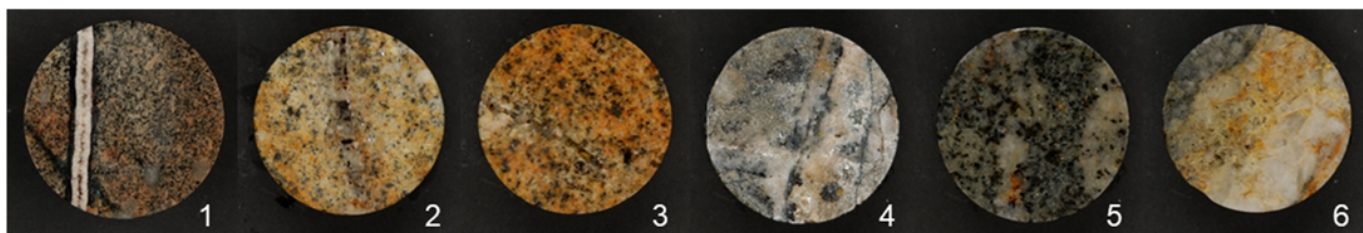


**Figure 1.** Simplified geological map of Cornwall, showing granite types after Simons et al. [5], sampling locations and relevant project locations; PTF simplified after Reinecker et al. [22]; meta sediments, dykes and non-magmatic geological units in grey.

## 2. Materials and Methods

The analysed rock samples are outcrop analogue samples (OAS). They were collected during fieldwork in June 2019 from six different locations of the Cornubian Batholith (selected from a total of 47 samples from 35 different locations—sea cliffs, major and minor natural outcrops, rock dumps and active and abandoned quarries) [23]. They have a relatively high geochemical conformity with the Carnmenellis Granite (based on data from Simons et al. [5]) and include mineralised veins, which allow analogies with hydrothermally altered zones around the faults and fractures of the PTF encountered in UD-1. As a result of a lack of sampling material from the granites of the Carnmenellis, Carn Marth or Carn Brea plutons, which contain veins, the representativity for the Carnmenellis granite is limited to far-field analogues (Land’s End, Tregonning Godolphin, Cligga and St. Austell plutons). Nevertheless, the present samples display an analogy to the fault and fracture zone itself. For analysis, the samples were cored into plugs 40 mm in diameter and ranging in length from 20 to 80 mm. Each core targets a vein, with the core axis drilled parallel to the vein (Figure 2). Cutoffs were ground to powder finer than 63  $\mu\text{m}$  for chemical and mineralogical analysis.

For comparison, drill cuttings from production well UD-1 from the open-hole section between 4 and 5 km MD are analysed. The cuttings, which were sampled by GEL/Geosciences Limited, represent 44 depth intervals of 10 m in length, between 4050 m TVD and 4930 m MD.



**Figure 2.** Top view on representative cores (40 mm diameter) from the six samples; the mineralogical composition of the sample and the veins is given in Table 1.

Besides an accompanying petrophysical analysis, the effect of chemical treatment on the permeability of the rock matrix and fracture systems due to acidification is investigated under approximation of reservoir conditions. This implies the acidification of samples using two methods (Core Flooding Tests, CFT; Autoclave Experiments, AE), a petrophysical before/after comparison and a geochemical analysis of the fluid–rock interaction.

A set of different analytical methods, such as XRF, XRD, AAS, IC, ICP-MS, thermoscaning, helium pycnometry, helium permeametry, water permeametry and sonic velocity, is used to characterise the samples petrologically and petrophysically before and after chemical treatment in AEs and CFTs at reservoir temperatures and pressures, as well as the spent acids from the AEs (Table 2, Figure 3).

In the chemical treatment experiments (AEs), the samples are placed in autoclaves together with acids at 150 °C for 24 h. The utilised acids are: (a) 15% HCl and (b) ‘white acid’, which consists of 12% HCl and 3% HF and resembles Regular Mud Acid (RMA), which is commonly employed in chemical well stimulation.

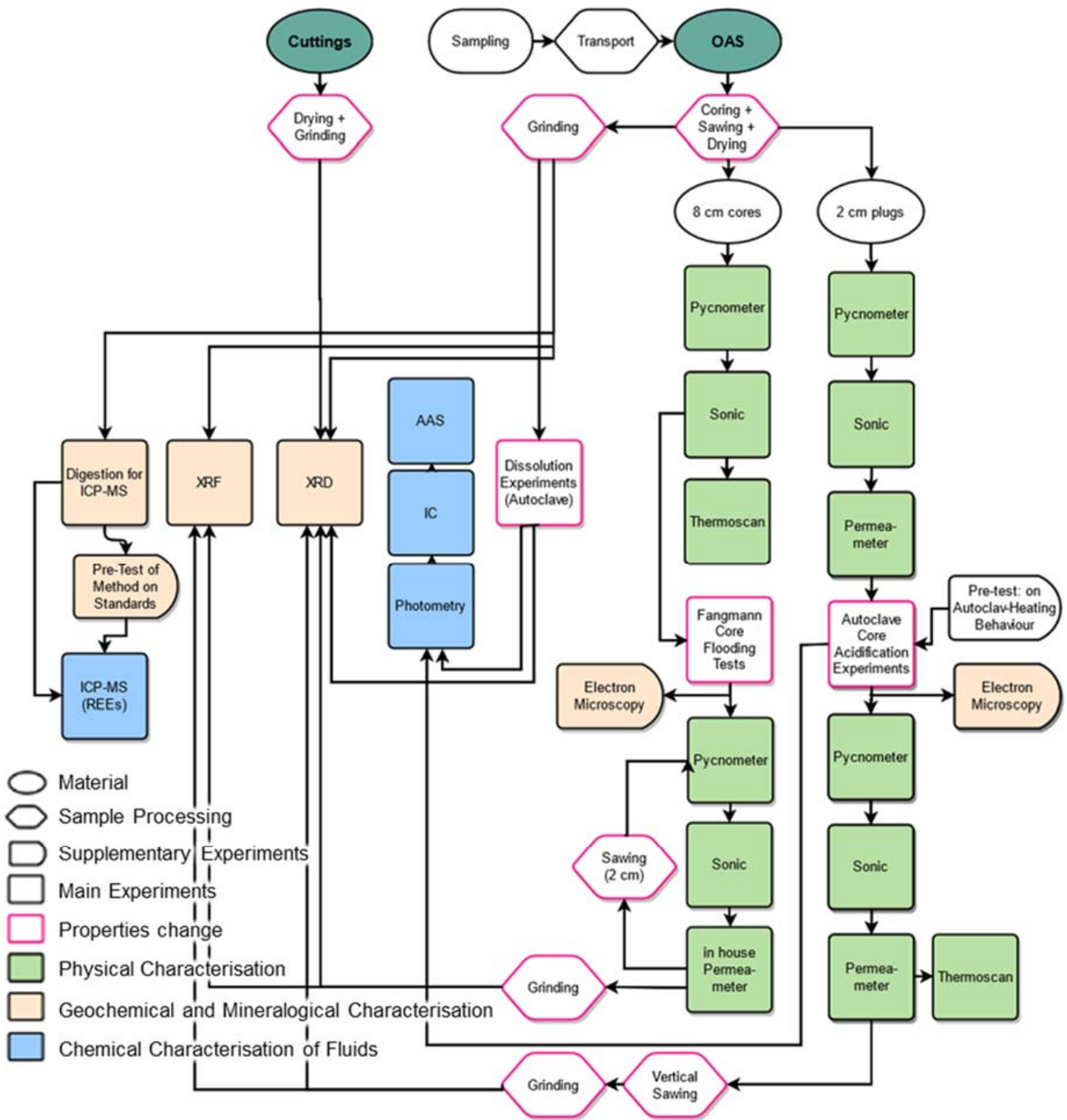


Figure 3. Flow chart of the lab work.

In the CFTs, which were conducted at the labs of Fangmann Energy Services (FES), the chemical blends SSB-007 and SFB-007 were circulated through the cores at a temperature of 150 °C and a confining pressure of 172 bar (2500 psi). During the flow rate-controlled tests, the differential pressure is logged to calculate the permeability development over time [24]. SSB-007 and SFB-007 have relatively similar characteristics to the fluids used in the autoclave experiments.

**Table 2.** Applied methods and analysed sample sets. Abbreviations: CFT = core flooding tests; AE = autoclave experiments; PEF = permeability enhancement factor; OAS = outcrop analogue samples.

Method	Sample Condition	Derived Parameters	Analysed Sample Sets
Gas pycnometry	Dry	Grain volume, grain density, porosity	All cuttings, all 8 cm cores, all 2 cm plugs, before and after acidification
Sonic	Dry	Seismic velocities, Young's modulus, Poisson ratio	All 8 cm cores, all 2 cm plugs and CFT cores, before and after acidification
Thermoscanning	Dry	Thermal conductivity, thermal diffusivity, specific heat capacity	All 8 cm cores, acidified 2 cm plugs
Gas Permeametry	Dry	Intrinsic permeability, permeability enhancement factor (PEF)	18 plugs before acidification, 12 plugs after AE, 5 plugs after CFT
Water Permeametry	Water- saturated	Permeability	5 plugs, sawn from the 3 acidised CFT cores
CFT	NH <sub>4</sub> Cl-saturated	Macroscopic changes, PEF	3 cores
AE: HCl, HCl + HF (powder)	HCl + HF saturated	Weight loss of sample	1 OAS powder sample with HCl, 6 OAS powder samples with HCl + HF, 1 OAS power sample with HCl
AE: HCl (plugs)	Partly HCl-saturated	Macroscopic changes	6 OAS plugs + 1 Blank
AE: HCl + HF (plugs)	Partly HCl + HF saturated	Macroscopic changes	6 OAS plugs + 1 Blank
REE-Analysis: Digestion, ICP-MS	Fluid	REE concentration	9 digested OAS powder samples + 2 Blanks + 13 Standards
AAS	Fluid	Element concentration	22 fluid samples (AE set 1, 2, 3)
IC	Fluid	Ion concentration	22 fluid samples (AE set 1, 2, 3)
Photometry	Fluid	Silicate concentration	22 fluid samples (AE set 1, 2, 3)
XRD	Powder tablets	Normalised mineralogical composition	9 representative OAS samples, 36 cuttings, 22 powdered samples after acidification (AE set 1, 2, 3 and CFT)
XRF	Pressed powder tablets	Normalised weight % of element or oxide concentration	9 OAS samples before acidification, 15 powdered plugs after acidification (AE set 2, 3 and CFT)

### 2.1. Sample-Preparation

All samples were dried to mass constancy (cuttings at 105° for 24 h, OAS at 65 °C for >48 h to avoid low-temperature alteration processes of clay minerals) and stored in closed containers at ~20 °C with silica gel. OAS were cored, sawn and burnished at the Institute of Applied Geosciences in Darmstadt. All cores have a diameter of 40 mm and include veins of different mineralogical composition. The initial length of the 'cores' was set to 80 mm (optimum: 2:1 length to width ratio), which had to be reduced to 20 mm 'plugs' for further experiments. The core axis was oriented parallel to the strike of the vein; the cores had plan-parallel surfaces. Grinding was performed in a tungsten carbide disc mill (two minutes at a speed of 1000 rpm) following Ferreiro Mählmann and Frey [25]. Grinding was performed on cuttings and core-cutoffs from sawing, which allow best comparability with OAS cores. The cutting samples lack the sub-63 µm-fraction, which includes the clay minerals (due to washing at the project site: rinsing 2–3 times and decantation of excess water through a 63 µm sieve without containment).

### 2.2. Petrophysical Methods

Gas pycnometry (determination of the effective porosity, which is an approximation of the total porosity, due to He diffusion) was conducted on all samples according to

the recommendations of Micromeritics [26] as described in Weydt et al. [27] with the two-chamber systems AccuPyc 1330, AccuPyc II 1340 and CorePyc 1360 (Micromeritics, Germany) using He. The bulk volume was calculated from the geometry of the cylindrical cores.

Sonic measurements were conducted as described in Weinert et al. [28] with an ultrasonic pulse generator (USG40) (Geotron-Elektronik, Germany), a PicoScope Detector and a UPG-S/UPE-S emitter/receiver set (pushed against the sample with a pressure of 1 bar, coupled by Magnaflux 54-T04 shear gel) on 80 mm cores and 20 mm plugs to calculate the dynamic Poisson ratio and dynamic Young's Modulus.

Thermal conductivity and thermal diffusivity were measured as described by Mielke et al. [29] on the 80 mm cores before treatment and on 20 mm plugs after treatment with a Thermal Conductivity Scanner (Lippmann and Rauen, Germany), using gabbro standards (TC) and Quartz/Titan and Titan/Steel standards (TD) [30].

The permeability was analysed with a column gas permeameter (stationary air permeameter with a Hassler type cell [31]). A verification of the results was performed with a water permeameter.

The gas permeameter measurements were conducted according to Filomena et al. [31], using the different pressure levels 1050–1250–1500–2000–3000–5000 mbar and a mantle pressure of 10 bar for each experiment. The pressure difference was set between up to 1000 mbar (samples with permeabilities in the range of  $10^{-17}$  m<sup>2</sup>) and only 50 mbar (permeabilities below  $10^{-14}$  m<sup>2</sup>). Further information about the method is provided by Weydt et al. [27]. Since the sample axis was parallel to the vein, the measured permeability was a combined vein and matrix permeability and the permeability of the whole sample was highly anisotropic.

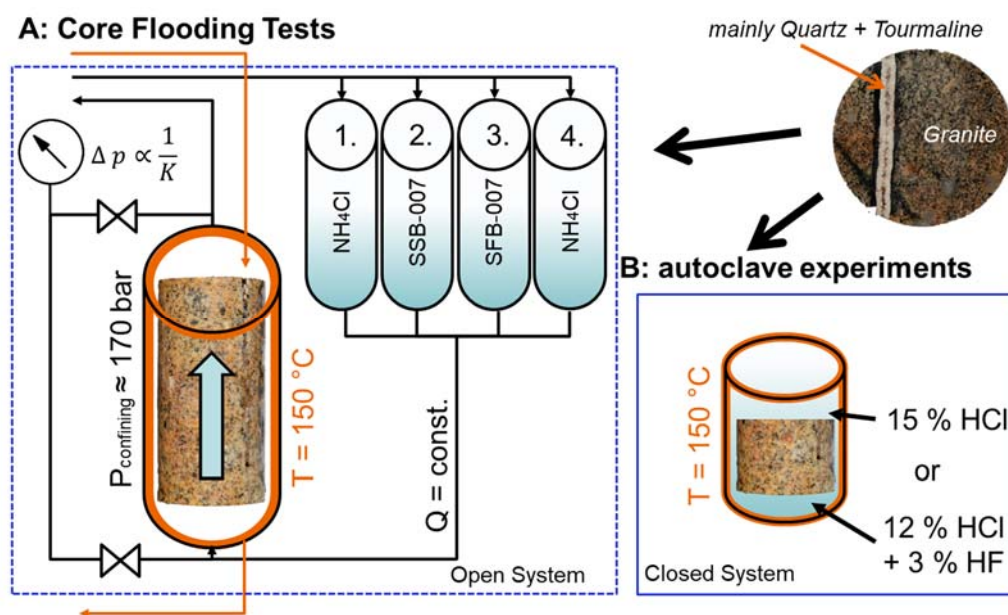
### 2.3. Acidification

CFTs were conducted at the labs of Fangmann Energy Services, using a Manual Reservoir Permeability Tester (OFI Testing Equipment) to induce and analyse changes to the sample properties caused by acidification (Figure 4). The relative permeability changes over time were analysed by the measurement of the pressure difference at the in- and outlet of the sample (constant flow rate; measurement similar to a permeameter). The CFT procedure can be summarised in the following steps:

1. 18 h pre-saturation of the core with NH<sub>4</sub>Cl (Ammonium-chloride solution with 50 kg NH<sub>4</sub>Cl per m<sup>3</sup> water) under vacuum conditions; installation of the sample in the permeability tester.
2. Pre-flush: Core flooding with NH<sub>4</sub>Cl and initial permeability measurement.
3. Acidification 1: Core flooding with SSB-007.
4. Acidification 2: Core flooding with SFB-007.
5. Post-flush: Core flooding with NH<sub>4</sub>Cl (flushing the spent acid and particles out of the core) and final permeability measurement.
6. Deinstallation.

The NH<sub>4</sub>Cl-brine was used because it has relatively similar flow properties compared to the applied acids and does not react with the acids, cores or the device. Besides, since NH<sub>4</sub><sup>+</sup> is not included in the geochemical analysis (and would be falsified anyway by the use of ammonium bifluoride as a constituent for the preparation of HF), the falsification of the analytical results was limited to Cl<sup>-</sup>.

The composition of Fangmann's acid blends SSB-007 and SFB-007 is confidential. According to general information from Fangmann, SSB-007 is based on HCl or on a Strong Organic Acid (SOA) with comparable reaction kinetics. SFB-007 contains additional HF and is relatively similar to Regular Mud Acid (RMA) [24]. RMA is a common acid used for sandstone matrix acidising [32]. Recalde Lummer and Rauf [24] state the applicability of Fangmann's product SFB-007 as well for granite.



**Figure 4.** Simplified sketch of the setup and conditions of core flooding tests (A) and autoclave experiments (B).

The applied test conditions were temperatures of  $150\text{ }^{\circ}\text{C}$ , confining pressure (mantle pressure, prevents lateral flow around the sample) of 172.4 bar and back pressure (system pressure, prevents boiling of the fluids) of 34.5 bar. A drive pressure pushed the fluid through the core and depended on the flow rate (sample 010006004: 0.9 mL/min through artificial fissure; 017001005: 1.36 mL/min through artificial fissure; 23001002: 0.665 mL/min through natural vein) and the permeability of the sample [24]. As the initial permeability of two samples was too low for the circulation of the brine, those samples were sawn along the original vein. This joint was compressed by the confining pressure. Further information on the permeability measurement before and after the CFTs is given in Appendix A.

Due to cost- and time-intensity and unknown composition of the acids, only three cores were analysed in CFTs and AEs were used to resemble the CFTs.

During the AEs, the acid and sample were encased in high-pressure autoclaves (Parr Acid Digestion Bombs, 302AC T304, Bomb No. 4748, stainless-steel autoclave system with a cylindrical Teflon (PTFE) container) and heated at  $150\text{ }^{\circ}\text{C}$  for 24 h (closed system). In contrast to the CFTs, no circulation of fluids through the sample was realised, implying that no pre- or post-flush was conducted to cleanse the samples of any reaction products after reaction (Figure 4).

In the autoclave experiments, two different acids were used to resemble Fangmann's acid blends SSB-007 and SFB-007:

- 15% HCl.
- 12% HCl with 3% HF (White acid, common basis for RMA, produced by mixing 1000 mL HCl (15%) and 50 g ammonium bifluoride (ammonium hydrogen fluoride,  $\text{F}_2\text{H}_5\text{N}$ , purchased as granulate) [33].

HF in a concentration range between 1 and 7% is dangerous to life in case of skin contact, among other hazards, and is class 2 in the German Water Hazard Classification System [34]. It is not biodegradable.

- For powder acidification experiments (set 1: 12% HCl + 3% HF) the autoclaves were loaded with 6 g of powder (from ground OAS) and 60 mL of acid (ratio of powder mass to acid volume: 1:10, assuming that the entire powder participates in chemical reactions with the acid) and rotated and shaken carefully.
- For core acidification experiments (set 2: 15% HCl and set 3: 12% HCl + 3% HF) the autoclaves were loaded with 40 mm diametral, 16–27 mm-high OAS plugs and



a volume of acid corresponding to the surface area of the plug in a ratio 1:1. This approach assumed that mainly the sample surface, plus permeable parts of the sample, mainly along the vein–rock matrix interface, would contribute to chemical reactions.

- To saturate the samples with the acids, the loaded Teflon cylinders were evacuated in a desiccator with a water-jet vacuum pump for 30 min.

After the heating phase, the autoclaves were cooled with wet tissue until they were cold enough to be touched and opened (approximately one hour, but as short a time as possible, to reduce precipitation). The liquid (spent acid) was then separated from the solid sample remnants for AAS and IC analysis via pipetting. The plugs were then rinsed with deionised water to allow safe handling and to reduce precipitation. For the powder samples, the non-dissolved solid fraction of the sample was repeatedly centrifugated with deionised water to increase the pH from pH < 1 to pH > 5, to allow safe handling of the sample and enable further analysis.

The following bullet points summarise the most important conditions of the autoclave experiments:

- Firstly, 15% HCl or 12% HCl + 3% HF.
- Plugs (surface to acid ratio 1:1) or powder samples (mass to acid ratio 1:10).
- 150 °C for 24 h.
- Ambient pressure (pressure increase only due to fluid expansion and reaction processes).
- No flushing of the samples during the experiment.

As the applied acids, especially at high temperatures, are very corrosive, the materials of the autoclaves and the Manual Reservoir Permeability Tester, as well as any used lab equipment in contact with the acids, had to be chosen accordingly and all devices and tools were visually controlled before and after use. With respect to the CFTs, the used acids contained corrosion inhibitors.

#### 2.4. Fluid Chemistry

Atomic Absorption Spectroscopy (AAS) was conducted with a ContraAA 300 (Analytic Jena, Germany, Xenon continuum source lamp plus monochromator, PTFE impact bead; acetylene/air-flame (2200 °C) or N<sub>2</sub>O/acetylene flame (2750 °C), measurement duration (3 to 4 s), flame height and the characteristic lines used for analysis depend on the element and are selected according to Analytic Jena recommendations, based on the software database; software Aspect CS, version 1.5.6.0). Further details on the method can be found in Broekaert, Skoog and Leary as well as Welz and Sperling [35–37]. The spent acids from the autoclave experiments were diluted by a factor of 50 or 100 as a reasonable compromise between the fitting with the calibration range and a reduction in the dilution error. This affects the measurement quality for Si, Al, Fe and partly Ca, K and Na. A six (or seven)-point calibration was conducted, with calibration standards from single-element standards (Carl Roth) and a LaCl–CsCl-solution (Merck KGaA, Germany) in a 2% HCl (supra quality) matrix.

Ion exchange chromatography was conducted with a Compact IC (Metrohm, Germany; Compact IC autosampler plus, two separation columns for an- and cations with organic polymer resin (both Compact IC plus; software MagIC Net™; cation-eluent: Pyridine-2,6-dicarboxylic acid (C<sub>7</sub>H<sub>5</sub>NO<sub>4</sub>) and nitric acid (HNO<sub>3</sub>), anion eluent: Sodium carbonate (Na<sub>2</sub>CO<sub>3</sub>)/Sodium hydrogen carbonate (NaHCO<sub>3</sub>). A 16-point calibration of the device is performed every three to four months, a control measurement is conducted within the analysis.

The silica content of the spent acid was determined with a Photometer Specord 200+ (Analytik Jena, Germany), and the reagents ‘Merck 14,794 (Silicate Test)’ using the software WinAspect+, according to DIN 38405-21 [38]. A nine-point calibration (0, 0.5, 1, 2, 3, 4, 5, 6 and 7 mg/L) was performed. Although the spent acid had a yellowish colour, the optical measurement was possible for set 1 and 3, as these samples were diluted by a factor of 1000;

set 2 was not measured because the required dilution factor was too high, as the silicate content is very low.

### 2.5. Mineralogy and Geochemistry

X-ray diffractometry (XRD) was conducted on powder tablets (low-texture samples) by Dr. R. Petschick (Goethe University of Frankfurt) with a Panalytical X'Pert Pro Powder X-ray-diffractometer (Kassel, Germany; Cu-ray tube with Cu radiation: 40 kV, 30 mA; Ni-filter with  $\lambda(\text{CuK}\alpha) = 1.542 \text{ \AA}$  (no separate  $\alpha$ -peaks), automatic divergence slits, X'Cellerator line counter) with the following goniometer settings: two hours per sample with a detection angle from  $2.5\text{--}70^\circ 2\theta$ , emitter and detector circuit step length of  $0.0083^\circ 2\theta$  and 100 s measurement time. The software X'Pert Data Collector (Panalytical, Germany), X'Pert Highscore Pro (Panalytical, Germany) and MacDiff [39] were used to evaluate the measurements; measured intensities were normalised with an external standard (Corundum), approximating the natural concentration. Fluorescence effects were reduced by a baseline correction and a peak-position correction was conducted based on the Quartz peaks. Further details on the method are described by Petschick [40].

For geochemical analysis the internal method 'Quant Express, Best Detection' (wavelength-dispersive, no external standards) of the X-ray-fluorescence-spectrometer S8 Tiger 4 kW (Bruker, Karlsruhe, Germany, scintillation counter for heavy elements, proportional counter for light elements (Bruker [41]) was used. For the evaluation, the total sum of measured elements was normalised to 100%.

For the powder tablets, a ground  $<63 \mu\text{m}$  sample was combined with Hoechst wax C micro powder ( $\text{C}_{38}\text{H}_76\text{N}_2\text{O}_2$ ) (Merck, Germany) in a ratio 1:4, homogenised in a rotator mixer for 30 min and pressed to tablets in a stainless-steel cylinder under pressure of 160 bar.

## 3. Results

Both acidification methods, CFTs and AEs, were used to analyse the permeability enhancement by chemical treatment (Appendix B, Figure A1) in samples from the Cornubian Batholith. Additionally, mineralogical, geochemical, petro- and thermophysical rock properties were determined, allowing before–after comparison and the quantification of the acidification effects. The OAS from the Cornubian Batholith were selected with focus on their comparability with the Carnmenellis granite and the presence of veins. The veins allowed comparison with hydrothermally altered zones in the well. Additionally, cuttings from the geothermal well UD-1 were used for a preliminary transfer of results from lab scale to the reservoir.

### 3.1. Sample Composition

All six sampled outcrops or quarries were granitic. However, as veins (mainly filled with Quartz) were targeted for sampling, all samples had elevated Quartz content compared to the cuttings from UD-1 and the regional chemistry, as described by Simons et al., (2016). In three cases the sample composition was classified as quartzolitic, as the volumetric overrepresentation of the veins caused elevated Quartz (and Tourmaline) content (Table 3). In relation to Plagioclase, the K-Feldspar content was also slightly elevated. As the resilience of Plagioclase is usually lower, compared to K-Feldspar, this may be an indicator for weathering effects on the samples. Macroscopically, Muscovite and Biotite were detected in all samples ( $\text{Ms} \geq \text{Bt}$ ). As accessory minerals, Tourmaline, Chlorite and Cassiterite were identified in the OAS and Hornblende and Chlorite in the cuttings. All veins consisted of Quartz, plus Tourmaline in most cases and rarely ore minerals. The general mineralogical evaluation of the samples with XRD confirms the macroscopically detected minerals, except for Biotite, which is underrepresented in the XRD results. The conducted REE analysis [42] generally correlates with the trends described by Simons et al. [5]. Detected deviations in REE may also be explained by weathering processes in the samples, because an inverse

Europium anomaly could be related to weathering of plagioclase. The REE evaluation might thus be useable as a tool to detect weathering.

**Table 3.** Composition of the six analysed samples. Mineral abbreviations according to Kretz [43].

Sample No. (MEETCW)	1 (001004)	2 (010003)	3 (010006)	4 (011003)	5 (017001)	6 (023001)
Minerals: matrix(macroscopic)	Qtz + Kfs + Pl + Ms + Bt	Qtz + Kfs + Pl + Ms + Bt	Qtz + Kfs + Pl + Ms + Bt + clay minerals	Qtz + Kfs + Pl + Bt + Ms	Qtz + Kfs + Pl + Ms + Bt + Toz?	Qtz + Kfs + Pl + Ms + Bt
Matrix grainsize	fine to medium	Fine	fine	fine	fine	fine to medium
Micas	Ms + Bt	Ms > Bt	Ms > Bt	Bt > Ms	Ms + Bt	Ms + Bt
Minerals: Vein(macroscopic)	Qtz/Tur/(Hem, reddish colour)	Qtz + Tur	Qtz	Qtz + Tur	Qtz (+ Tur)	Qtz, ore mineral (Cst)
Minerals: entire sample (XRD)	Qtz > Pl > Kfs > Ms > Tur	Qtz > Kfs > Ms > Pl > Tur	Qtz > Kfs > Ms > Pl > Tur	Qtz > Ms > Kfs > Tur	Qtz > Ms > Tur > Pl > Bt	Qtz > Ms > Bt > Tur > Chl (> Cst)

### 3.2. Acidification

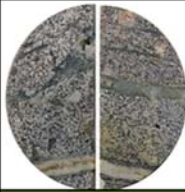
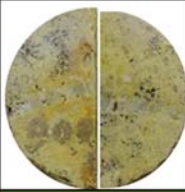
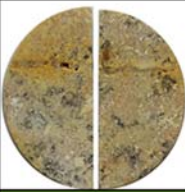
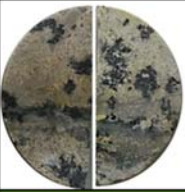
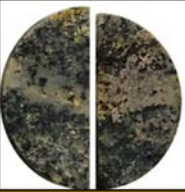
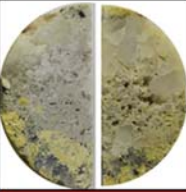
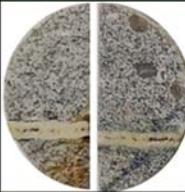
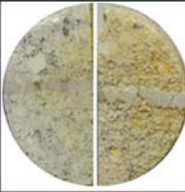
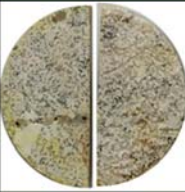
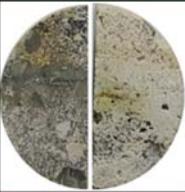

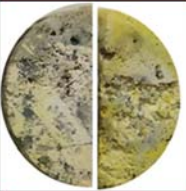
The CFTs, conducted and evaluated by Fangmann Energy Services [44], resulted in a significant increase in permeability. To quantify the effectivity of the acidification, we defined the permeability enhancement factor (PEF), which is the ratio between the permeability before ( $K_{pre}$ ) and after ( $K_{post}$ ) treatment:

$$PEF = K_{post}/K_{pre} \quad (1)$$

The CFTs resulted in a PEF between 4 and 50. On the treated samples, a white precipitate was visible after the acidification.

In contrast to the CFTs, the trend in permeability variation was more ambiguous in the AEs. The AEs induced a permeability variation by a PEF between 0.1 and 40 (for 15% HCl: 0.8–39.44; for 12% HCl + 3% HF: 0.13–40.48). A permeability decrease (PEF < 1) was, in most cases, accompanied by (and likely caused by) the precipitation of a yellowish and a white mineral, which were macroscopically visible on the plugs (Figure 5). After treatment with HCl + HF, the bottom of the samples showed more intense changes: a relief was created, which was especially visible in samples 2, 3, 5 and 6 (Figure 5). In this relief, the Quartz veins acted as the resistant parts and remained almost unaffected. In sample 3, this effect was visible for the Quartz grains in the matrix. On the top of the sample, these effects were less intense. In addition, samples 2 to 6 showed yellow or white precipitation, also mainly on the bottom of the samples. After treatment with HCl, a relief was only created in sample 2, 5 and 6, mainly close to the veins. No white precipitates were visible, but yellow precipitates occurred on sample 2 to 6.

The yellow mineral does not resemble any original crystal structures and can partially be dissolved or washed away, but reprecipitates during the drying process (65 °C). This is most likely caused by the evaporation of the remaining pore fluid and indicates that the acid penetrated the sample surface. This was confirmed by a reaction front, which was visible in most samples in the cross section of the plugs after sawing them vertically. This reaction front was commonly located around the vein (sample 1, 4, 5 and 6) or in the entire sample (sample 2 and 3), but with a gradual increase towards the vein. The white mineral mainly occurred on or along pre-existing minerals (Feldspars and Quartz), especially on the bottom of the plugs. In difference to the yellow reaction front, it did not seem to be related to the veins and occurred only on the outside of the samples. The precipitate occurred in spent 15% HCl as well as 12% HCl + 3% HF.

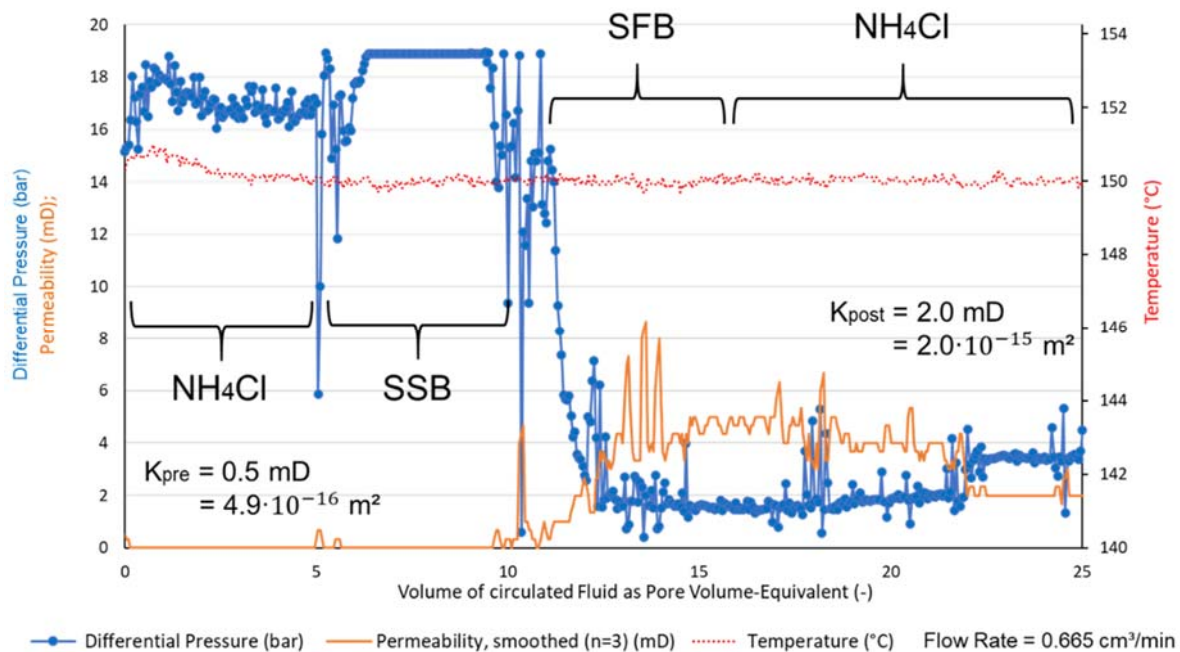
15 % HCl						
	1.94	1.07	39.44	1.63	1.00	0.80
12 % HCl + 3 % HF						
	7.07	0.13	40.48	0.16	22.58	0.59

**Figure 5.** Photomontage of the plugs after acidification, combined with the permeability enhancement factor resulting from treatment with the respective acids 15% HCl or 12% HCl + 3% HF in autoclave experiments: top and bottom view of the sawn plugs after the autoclave experiments illustrating the stronger degree of precipitation on the samples bottom surfaces.

In the fluid samples, no precipitation processes were observed, even after several weeks of storage. During the AEs, the acid colour changed from clear transparent to an intense yellow. Based on the hydrochemical analysis of the spent acid, showing elevated iron concentrations, most likely these minerals were partly iron hydroxides (FeO(OH), Goethite or Limonite). Macroscopically this was indicated by the yellowish colour of the fluids, which could be interpreted as an indicator for hydrated trivalent iron, as the iron(III) complex  $[\text{FeCl}(\text{H}_2\text{O})_5]^{2+}(\text{aq})$  (ligand  $\text{Cl}^-$ ) was yellow [45]. The precipitate may also include silica gel. According to Portier and Vuataz [46] this is formed by a secondary substitutionary reaction of hexafluorosilicic acid (high solubility) (which is formed from HF-acidification of Quartz) where Si ions are exchanged by  $\text{Al}^{3+}$  and precipitate as  $\text{SiO}_2$ , while the fluoaluminates remain in the solution. This reaction is triggered when HF is nearly consumed. As clays or Micas are the main source for the  $\text{Al}^{3+}$ , they increase the probability of silica gel precipitation.

Permeability tracking during the CFTs, as displayed in Figure 6, shows the processes during the acidification. Regarding the evaluation of the CFTs, the tracked pore volume can be considered proportional to time, since the flow rate was constant. As visible in Equation (A1) in Appendix A, the pressure difference was inversely proportional to the permeability and the maximum measurement range of the device is approx. 19 bar. The sudden drop in measured pressure difference at the transitions between the different fluids, which was visible in all three CFTs, was caused by an inlet pressure drop when the fluid valves were changed. Regarding sample 6 (Figure 6), the effect of SSB-007 was insignificant in the sample (no calcite or well-soluble minerals), as the differential pressure did not vary before and after SSB-007. During the application of SSB-007, differential pressure decreased, implying a high efficiency of HF in this sample. The shape of the curve resembled an exponential decrease, implying a fast efficiency decrease in HF. In the sample this effect could be due to an initial dissolution phase, which mainly affects pore throats and macropore contaminants. Combined with the flushing of the macropores and smaller pores, now with extended pore throats, the removal of particles increases the permeability with high effectivity in this initial phase. Another explanation might be that the exponential decrease was an effect of grain integrity and grain size distribution. Because this samples showed signs of weathering, the trend could express a significant reaction with fine- to

very fine pre-damaged grains. After this, the grains with higher integrity showed a lower reactivity with SFB-007. In the post-flush phase, the pressure difference increased after the circulation of 22 pore volumes. This behaviour might indicate the collapse of a fracture under the applied confining pressure during the flushing process. This implies the risk of a permeability decrease by the reduction in rock stability during chemical treatment. In further CFTs, permeability increased during the post-flush phase displayed the relevance of the post-flush, which seemed to mobilise particles that cause pore clogging.

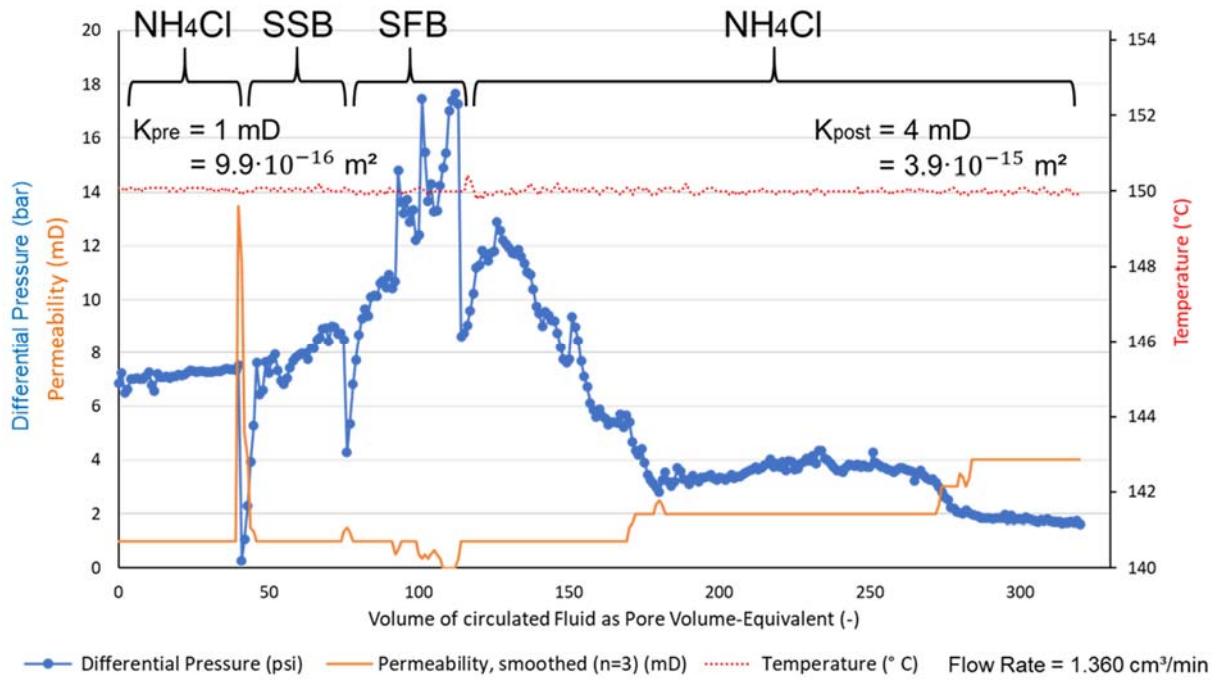


**Figure 6.** Pore volume—differential pressure diagram showing the development of the CFT on sample 6, applied flow rate: 0.665 mL/min; modified after [44].

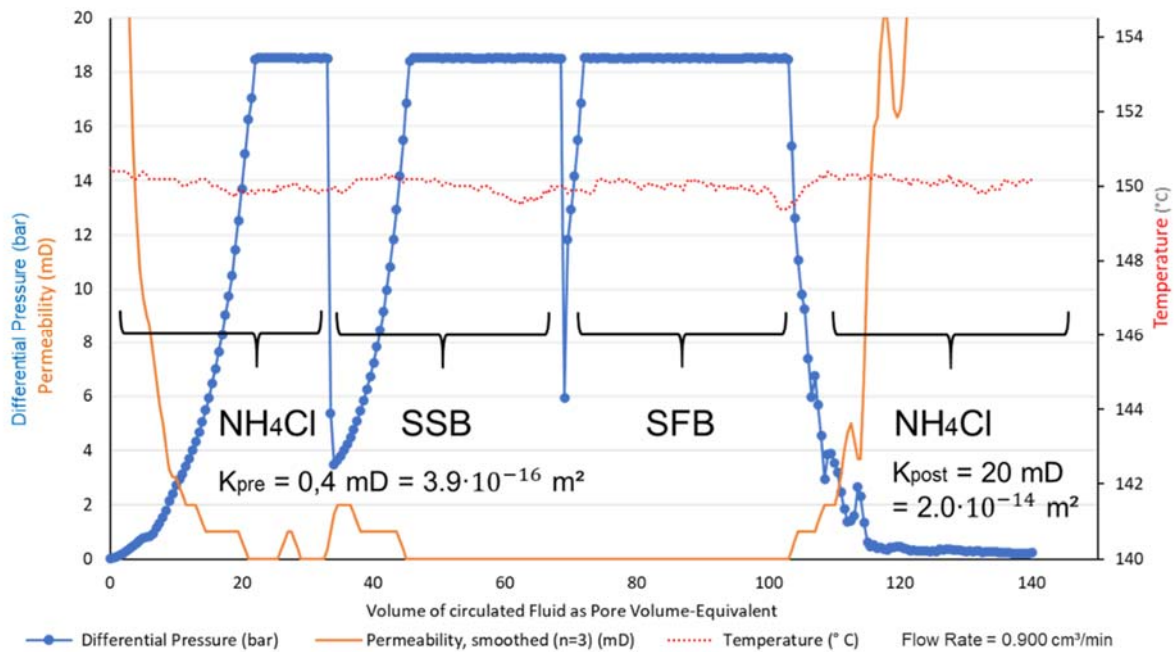
In difference to sample 6, the samples 5 (Figure 7) and 3 (Figure 8) were sawn vertically along the natural vein to increase the permeability, because the execution of the CFTs was not possible as the initial permeability was too low for circulation of ammonium chloride.

The documented pressure differences in the CFT on sample 5 resemble sample 6. A major difference is that during the long post-flush period, the pressure difference decreased significantly after a total of approximately 275 PV of circulated fluids and the permeability increased, respectively (doubling of the permeability from 1 mD ( $9.87 \times 10^{-16} \text{ m}^2$ ) to 4 mD ( $3.95 \times 10^{-15} \text{ m}^2$ )). This implies a high relevance of the post-flush, which seems to mobilise particles, that cause pore clogging.

The evaluation of sample 3 shows major difficulties during the CFT. The permeability of the sample, even after sawing an artificial vein, was too low to allow the analysis of the pressure differences, because the device's measurement range is exceeded. The given diagram cannot be analysed with regard to the effectivity of the acid blends, but a general statement about the acidification is still possible: the permeability increases significantly, since a low-rate circulation of ammonium chloride becomes possible after the acidification.



**Figure 7.** Pore volume—differential pressure diagram showing the development of the CFT on sample 5, applied flow rate: 1.360 mL/min; modified after [44].



**Figure 8.** Pore volume—differential pressure diagram showing the development of the CFT on sample 3, applied flow rate: 0.900 mL/min; modified after [44].

This implies a significant permeability increase in all three cases, which is almost exclusively caused by SFB-007. The flushing of the pores was identified as an important factor to increase the permeability after the acidification but may result in a pore collapse due to the confining pressure.

The three CFT diagrams show that the permeability increase could account for the HF-bearing acid blend SFB-007, while the effect of SSB-007 was insignificant in the samples.

The relevance of SSB-007 was mainly as a pre-treatment to avoid unwanted chemical reactions with HF, such as the precipitation of  $\text{CaF}_2$ . In the AEs, the PEF was higher if HF was involved, but the number of cases with permeability decreased as well. Hydrochemical analyses, using AAS, IC and Si-Photometry, show that the total ion load of the spent HF-based acid was far higher compared to spent 15% HCl. The precipitation of the iron hydroxide was most intense in samples with the highest ion load in the fluid.

### 3.3. Petrophysical Methods

Permeametry, Sonic, Thermoscanning and Pycnometry were used to assess the petro- and thermophysical rock properties before and after treatment. The initial gas-permeabilities of the untreated samples ranged between  $1.3 \times 10^{-18}$  and  $3.1 \times 10^{-14}$   $\text{m}^2$ . After treatment, the gas permeabilities ranged between  $1.2 \times 10^{-17}$   $\text{m}^2$  and  $1.8 \times 10^{-14}$   $\text{m}^2$ . The permeability correlated with the porosities, which ranged between 0 and 12.02% before treatment and increased to 0.92 to 14.52% after treatment. The largest porosity increase was achieved during the CFTs (max. plus 5.03%). In the AEs the treatment 12% HCl + 3% HF was more effective than 15% HCl. Thermal conductivity ( $2.5\text{--}4.5$   $\text{W}\cdot\text{m}^{-1}\cdot\text{K}^{-1}$ ) and thermal diffusivity ( $1.2\text{--}3.9 \times 10^{-6}$   $\text{m}^2/\text{s}$ ) resulted in specific heat capacities between 572 and 827  $\text{J}\cdot\text{kg}^{-1}\cdot\text{K}^{-1}$  and were not significantly affected by acidification. Sonic velocities (p-wave velocities between 3095 and 6360 m/s, s-wave velocities between 1909 and 4447 m/s, mean value per sample before treatment) resulted in high Young's moduli and low Poisson ratios. These deviated from the literature, possibly because Quartz veins provide preferential wave propagation paths. While the Poisson ratio decreased after acidification, Young's modulus increased, indicating that precipitation might have increased the mineral interconnectivity.

## 4. Discussion

As a major difference between the CFTs and the AEs, in the CFTs the applied acids SSB-007 (based on a strong organic acid), followed by SFB-007 (based on hydrochloric acid plus hydrofluoric acid) were circulated through up to 80 mm long cores for up to 2.5 h under approximation of reservoir conditions (150 °C, 172.4 bar confining pressure). In contrast, in the AEs, the acids 15% HCl or 12% HCl + 3% HF, together with 20 mm long rock plugs or powder from ground samples, were heated to 150 °C for 24 h without circulation. This implies that no pre- or post-flush was conducted.

The analysis of the effectivity of the acids regarding different minerals, quantified by using XRD and XRF as well as AAS, IC and Si-Photometry on the spent acids, displayed similar trends, which generally correlate with earlier studies [46,47] as well as with results from Economides and Nolte [48].

The most relevant chemical equations for reactions with HCl + HF are listed below to give a preliminary understanding of the results discussed in the following section. Chemical reactions with only HCl are not displayed separately since, chemically,  $\text{Cl}^-$  has comparable characteristics to  $\text{F}^-$  and can therefore be involved in similar chemical reactions, but with reaction rates that are several magnitudes lower. The following chemical equations were documented by Economides and Nolte [48]:

- Quartz  $4\text{HF} + \text{SiO}_2 \Leftrightarrow 2\text{H}_2\text{O} + \text{SiF}_4$  (silicon tetrafluoride)
- $\text{SiF}_4 + 2\text{HF} \Leftrightarrow \text{H}_2\text{SiF}_6$  (hexafluorosilicic acid)
- Na-feldspar  $\text{NaAlSi}_3\text{O}_8 + 14\text{HF} + 2\text{H}^+ \Leftrightarrow \text{Na}^+ + \text{AlF}_2^+ + 3\text{SiF}_4 + 8\text{H}_2\text{O}$
- K-feldspar  $\text{KAlSi}_3\text{O}_8 + 14\text{HF} + 2\text{H}^+ \Leftrightarrow \text{K}^+ + \text{AlF}_2^+ + 3\text{SiF}_4 + 8\text{H}_2\text{O}$
- Calcite  $\text{CaCO}_3 + 2\text{HF} \Leftrightarrow \text{CaF}_2 + \text{H}_2\text{O} + \text{CO}_2$

Depending on the respective stoichiometry, clay minerals reacted with HF +  $\text{H}^+$  under the creation of  $\text{AlF}_2^+$ ,  $\text{SiF}_4$  and  $\text{H}_2\text{O}$  in different ratios. As the composition of Tourmaline is extremely variable, no chemical reaction was provided.

While the reactions between HF and silicates generally resulted in the creation of liquid hexafluorosilicic acid, which, depending on the pH of the resulting fluid, could precipitate as amorphous silica gel, a reaction between HF and Calcite would immediately result in the precipitation of  $\text{CaF}_2$  and cause pore clogging.

The XRD results show that on ground samples 12% HCl + 3% HF, the Quartz content in the treated samples increased to up to 100%. This implies that every other mineral reacted entirely. An exception is Tourmaline (Schorl), which was partly persistent in samples with an initial concentration above 5.5%. As a product of the HF acidification, Hieratite ( $K_2[SiF_6]$ ) crystallised in several samples. In accordance with results from Sclar and Fahey [49], it was most likely a product of the acidification of K-Feldspars, since it contains K and F and was found in the samples with initially highest K-Feldspar concentrations. In the powder samples, Micas and Plagioclase were dissolved completely, but no correlation reaction products could be identified. The crystallisation of further minerals is indicated with additional spectral peaks in the XRD-results, but those minerals could not be identified, as well as amorphous phases. In the acidified rock samples (plugs) trends were less distinctive. For 12% HCl + 3% HF as well as 15% HCl, Quartz and Tourmaline were least affected, while Micas, especially Fe-Chlorite, were statistically most affected. The Feldspar contents did not display clear trends, but in relative numbers Plagioclase seemed to be less affected than K-Feldspar. If 15% HCl was applied, the effect on Quartz was insignificant. In all samples the effectivity of the acidification regarding the relative mineral concentrations increased if HF was involved. Comparing the SSB-007 plus SFB-007 acidification in CFTs with 12% HCl + 3% HF in AEs, the trends were similar, except for Muscovite, which seemed to be less affected. This may be related to additives with the purpose of inhibiting the participation of clay minerals.

The XRD results were generally confirmed by the XRF results, which displayed low to no effectivity regarding Quartz, depending on the acid, (relative  $SiO_2$  increase) and higher effectivity regarding Micas and Feldspars or other Al-bearing silicates (relative  $Al_2O_3$ ,  $K_2O$  or  $Na_2O$  decrease). The effectivity regarding Schorl was low to intermediate ( $Fe_2O_3$  concentration decreased or did not change in samples without Fe-Chlorite and Biotite). Again, the trends accounted for 15% HCl as well as for 12% HCl + 3% HF, but the magnitude was larger for 12% HCl + 3% HF. Further trends in other main elements ( $TiO_2$ ,  $MnO$ ,  $MgO$ ,  $CaO$ ,  $Na_2O$ ,  $K_2O$ ,  $P_2O_5$ ) or trace elements cannot be generalised.

In sample 6 (023001, Cligga granite), as an exception, indicators for Cassiterite, Galena, Pyrite or other ore minerals were detected. This confirms the XRD results and macroscopic observations for the specific sample.

The chemical analysis of the spent acids, using AAS, IC and Si-Photometry also confirmed the trends from XRD and XRF. In most cases, relative concentrations can be generalised as trends for the respective acidification set:

- 12% HCl + 3% HF, 150 °C, powder: Al > Si > Na > Ca > K > Ti > Mg > Fe > Mn
- 15% HCl, 150 °C, plugs: Mn > Al > Fe > Ti > Ca > K > Mg > Si
- 12% HCl + 3% HF, 150 °C, plugs: Al > Na > Fe > Si > Ca > K > Mg > Ti > Mn

Regarding 12% HCl + 3% HF as well as 15% HCl acidification on plugs, the relative participation rates of Feldspars are low (relatively low  $K^+$ ,  $Na^+$  and  $Ca^{2+}$  concentrations), while Micas, especially Muscovite, are strongly affected (relatively high  $Al^{3+}$ -concentrations). Tourmaline and other Fe-bearing minerals have intermediate relative participation rates, if present (relatively high  $Mn^{2+}$  and  $Fe^{2+/3+}$  concentrations). If 15% HCl is used, Si is absent in the fluid, implying zero participation of silicates. This is a contradiction to the abovementioned results unless assuming precipitation of silica gel, as described above. In contrast, applying 12% HCl + 3% HF (comparable trends on plugs as on powder), the participation of Feldspars and Micas, as well as mafic minerals, is magnitudes higher compared to 15% HCl (extremely high  $Al^{3+}$ , high Si and high  $Fe^{2+/3+}$ ,  $Mg^{2+}$ ,  $Ca^{2+}$ ,  $Na^+$  and  $K^+$  concentrations). Total ion loads reach up to approx. 11,000 mg/L in spent 12% HCl + 3% HF, but only approx. 550 mg/L in spent 15% HCl.

Comparing the acidification on plugs and powder (with 12% HCl + 3% HF in both cases), the data show similar trends. In relative numbers, the ratio of the dissolved elements fits quite well between acidised OAS powder and plugs. The main difference is an extremely low  $Fe^{2+/3+}$  concentration in the fluid from powder acidification experiments (maximum  $Fe^{2+/3+}$  concentration in powder experiment: 16 mg/L; in plug experiment:



1355 mg/L). This might indicate the precipitation of an iron mineral on the large powder surface and separation during centrifugation of the powder sample. In XRD, the respective mineral would likely not be detected as the precipitate would most likely precipitate as an amorphous mineral. No XRF measurements of the powder samples were performed, because the remaining material mass was too small for the method.

Summarising the effects on specific minerals, the effectivity of the acidification depends primarily on the composition of the spent acid. Theoretically, the effect of the temperature is relevant, but since all experiments were conducted at the same temperature, this cannot be validated by the data. The effect of the grain size is minor, as powder and plug acidification had comparable effectivities regarding different minerals, although the grain size was homogenised by pulverisation. It also depends on geochemical variations in the sample, such as varying concentrations of ore minerals, Chlorite, Muscovite and Biotite or Tourmaline. Feldspars and Mica are mainly affected by the chemical reactions. The effect on Quartz is far lower, even if HF is involved. Since the AEs last 24 h and near-equilibrium conditions are established, reaction kinetics are not as important for the resulting effects on the samples as they would be in a real stimulation or in CFTs, in which the reaction time is much lower (0.5 to 6 h). However, since all relevant reactions imply an activation energy threshold, reaction kinetics still influence the results. Equilibrium constants in a multi-phase—multi-component system can be derived from reaction rate constants. Portier and Vuataz [46] use respective parameters for a granite system and state that, using 12% HCl + 3% HF, the reaction rates for Feldspars and Micas are two magnitudes higher than for Quartz. Their results also confirm a higher reactivity of K-Feldspar compared to Plagioclase. Reaction rates for HCl and HCl + HF in varying concentrations are also provided by Economides and Nolte [48] and confirm the present results. If the effectiveness of the acids is summarised in terms of the estimated solubility of the minerals, which are predominantly involved in the analysed samples, the following order can be derived:

- Micas (especially Fe-Chlorite) > K-Feldspar > Plagioclase > Tourmaline > Quartz

Further quantifications of the reaction kinetics in the autoclave experiments would require a larger dataset and more detailed analysis. Regarding SSB-007 and SFB-007, reaction kinetics are influenced by the addition of retardants and corrosion inhibitors. As the exact composition of the acid blends has not been provided, no further interpretation of the reaction processes during the CFTs is possible.

Regarding the comparability of the acidification methods (CFTs versus AEs; 15% HCl versus SSB-007; SFB-007 versus 12% HCl + 3% HF), it is very important to consider the different reaction times, as the SSB-007 flush lasted less than one hour in the CFTs, while the AEs were conducted during 24 h. As a summarising comparison, 15% HCl has a weak, but evident effect on the AE samples and in the fluid samples, while SSB-007 did not cause any effect on permeability that could be identified during the CFTs. All effects related to geochemical variations induced by the CFTs could solely account for SFB-007. Comparing SFB-007 and 12% HCl + 3% HF, the effects seem to be quite comparable, except for the slightly lower effectivity of SFB-007 on Micas, detected in the XRF data. From several papers published by Fangmann Energy Services, only Recalde Lummer and Rauf [24] unambiguously describe the application of SFB-007, stating that K-Feldspars of the analysed samples are not affected by conducted experiments. This is not confirmed by the present results. The absolute effectivity of both methods is not comparable due to the differences in duration, pressure and the acid circulation in the CFTs.

The most important limitations of methods are related to the acidification experiments: in the CFTs, no absolute permeability is measured since the fluid properties (viscosity of the acid, as well as the exact composition of the acid blends) are unknown and likely change during the experiment. Thus, unfortunately, the permeability determination is only reliable during the ammonium chloride flush. The dynamic viscosity of ammonium chloride under test conditions would need to be determined, as well as the fluid properties of SSB-007 and SFB-007, which are required for hydraulic modelling. The flow behaviour, and thus also the retardation and reaction behaviour, is highly dependent on viscosity and density. In the

AEs, the quantification of the mineral dissolution is corrupted by precipitates, which do not occur in the CFTs to a comparable extent and would not occur in the near-well regions of the reservoir (metres to tens of metres), if an adequate post-flush is conducted to displace the reaction products deeper into the formation. This displays the main limitation of the AEs.

Indicators for the relevance of ore minerals in acidification are found in sample 6 (023001), where precipitates are most abundant. The thickness and the extent of the yellow to white precipitate is highest. Uniquely, sample 6 contains macroscopically visible fine-grained ore minerals. Cassiterite was identified by XRD; further ore minerals (possibly Galena and Pyrite) are indicated in XRF data. The AEs on sample 6 result in a PEF of 0.8 for 15% HCl and 0.59 for 12% HCl + 3% HF. It is the only sample with a permeability decrease after acidification with 15% HCl. Fe was identified to cause the yellow precipitate, which occurs not only in the presence of ore minerals but also in samples that contain mafic or Fe-rich minerals, such as Schorl, Hornblende or Fe-Chlorite. Assuming the presence of Pyrite, the abundance of the precipitate can be explained. In the XRF data, the relative Fe<sub>2</sub>O<sub>3</sub> content increases, indicating that Fe-ions reprecipitate. To assess the presence of ore minerals for a chemical stimulation, XRF is recommended instead of XRD, as XRD is not a well-suited method to identify ore minerals.

Comparing OASs and cuttings, only limited transferability is given between the two sample types. This highlights the significant effect of surface weathering or alteration processes on the samples, which can be excluded by the drilling of Side Wall Cores for a high-quality assessment of the reservoir. The reduced normalised Plagioclase content in the OAS, in comparison to the cuttings, could be another indicator—besides the REE pattern—for weathering, because Plagioclase has higher weathering rates than K-Feldspars. Nevertheless, the mineralogical composition of the OAS resembles hydrothermally altered fracture zones and is therefore a relevant approach for deep geothermal systems in fractured granite.

## 5. Conclusions

Regarding the results of the present study, the most efficient acid for United Downs is clearly HF-based. In other wells, when calcite is present in veins, HCl or an Organic Acid is usually sufficient for stimulation, but this is not the case in UDDGP. In case chemical treatment is not an option, e.g., due to regulatory requirements regarding the applied acids, pulse fracturing treatment—as described by Tariq et al. [50]—might be an option. Thermochemical acid fracturing, as described by Tariq et al. [51], which is based on the pressure increase during specific chemical reactions and can be based on less hazardous chemicals, may also display an alternative. HF is not biodegradable and not environmentally friendly, although Recalde Lummer and Rauf state that the treatment system SSB-007 + SFB-007 is biodegradable [24], which is confirmed by the safety sheets of the single components. To reduce safety and environmental risks, the HF-based acid is prepared on site from ammonium bifluoride and strong organic acids, which are less hazardous. This allows safer handling and a demand-controlled preparation of the required acid volume. Technical restrictions regarding the project site, such as swelling of clays and compatibility with borehole and reservoir fluids, as well as casing steel and cements were analysed and show no signs of incompatibility. Technical constraints from the environmental side include the presence of a hydraulic barrier, such as a customised barrier (e.g., inert, impermeable textiles or foils) on top of a concrete pad of sufficient extent around the well, the integrity of the well cementation, the exclusion of any leaks in or around the well or project site and the exclusion of any other hydraulic links between the reservoir and non-target areas.

The CFTs were conducted to approximate a chemical reservoir stimulation on lab scale. A major difference between the lab-scale experiments and a reservoir stimulation is that in a reservoir stimulation, chemical stimulation is accompanied by hydraulic and thermal stimulation effects.

As relatively cold fluids, compared to the reservoir temperature, are injected, thermoelastic effects may cause fracture opening or fracturing as well, as significant contraction effects may occur due to the large reservoir volume and will strongly be influenced by injection volume and the duration of injection. In the CFTs, the sample is heated to 150 °C, while the fluid is at room temperature before the contact with the sample. For the small core volume, thermal contraction is not relevant. Effects of thermal contraction would most likely occur during the ammonium chloride pre-flush but have not been detected.

The hydraulic pressure is at least the hydrostatic pressure of the fluid column in the well, but may be artificially increased, depending on the stimulation approach.

Regarding the pressure conditions, the applied confining pressure in the CFTs was set to 172.4 bar and a back pressure of 34.5 bar was applied to prevent boiling of the fluids. The pore pressure was in a dynamic relation with the measured differential pressure and depended on the pump pressure, which varied to maintain a constant flow rate (OFITE 2019). In comparison, the stress conditions in the production well were strike-slip stress conditions (max. horizontal pressure > vertical pressure > min. horizontal pressure), critically stressed for shearing on pre-existing fractures with matching orientation [22]. Indicators for a change of stress regime in the open-hole sections were found and are described by Reinecker et al. [22].

While the CFTs affect a specific fissure or vein, a reservoir stimulation is conducted with packers or coiled tubing, affecting entire well sections. The fluid follows preferential flow paths, which implies the risk of creating wormholes along the most permeable fractures, while closed fractures might only be affected by the acid to a very low degree. This issue should be investigated in further studies, e.g., by digital rock imaging, as well as quantification of the changes in roughness.

In the CFTs, during the flushing process under the applied confining pressure, a fracture collapse was detected, as described in Section 3.2. This risk is transferable to the reservoir, as it implies the risk of a permeability decrease by the reduction in vein or fissure stability by particle washout or during chemical treatment. In hydraulic stimulations, proppants are commonly used to avoid fracture collapse. In the case of the granitic reservoir rocks, the Quartz grains, however, might act as natural proppants and keep the fractures open, while Micas and ore minerals in the fractures are preferentially dissolved.

The dissolution characteristics for a HF based acid are good, but imply the precipitation of pore-clogging minerals. A post-flush needs to be executed, which ensures that precipitation occurs only in the reservoir at greater distance of the well, minimising negative hydraulic effects to the well productivity. As an attempt to quantify the required post-flush volume for chemical treatment, it should correspond to at least one times the pore volume of the sample. With respect to the possible fracture collapse and pressure limitations due to technical and safety constraints, the maximum post-flush volume is limited as well. In view of these limitations, a post-flush of three to five times the pore volume is recommended.

Chemical stimulation with HF is common in petroleum projects and has also been applied in geothermal projects [52–54], but open-access datasets are scarce. HF-treatment involves severe risks for human health and the environment. The company and operator have to ensure that during chemical treatment, all risks to health and the environment are considered. Procedures to handle the fluids have to be designed accordingly and countermeasures need to be in place to be applied immediately if needed. The acid blend SFB-007 has already been applied in geothermal projects with granitic reservoir rocks as Soultz sous Forêts, Rittershoffen and Vendenheim [24]. An intense pre-stimulation assessment of the reservoir is required to search for the optimum acid blends and to define required volumes or technical alternatives. The presented research contributes to the optimisation of stimulation pre-assessment, which is transferable to other projects in fractured crystalline rock. The present work contributes significantly to the stimulation pre-assessment for the United Downs Deep Geothermal Power project and therefore improves the planning process of the reservoir treatment. It complies with the MEET project objective to optimise chemical treatment and reservoir assessment. SSB-007 + SFB-007 are innovative,

state of the art acid blends, which are applied internationally. The approximation of these acid blends with 15% HCl and 12% HCl + 3% HF has proven to be a suitable approach. Elaborated results from the selected samples can be transferred to further project sites in a fractured granitic basement. The applied methods in the compiled workflow are an innovative, well-suited tool set for a generalised approach to the lab scale assessment of rock acidification, particularly for application in a crystalline basement.

Using a set of laboratory tests that, to our knowledge, have never before been performed with similar acid combinations on granitic rocks for geothermal purposes, the present study provides new insights into the efficiency as well as possible difficulties of chemical stimulation in such rock types.

**Supplementary Materials:** The following are available online at <https://doi.org/10.48328/tudatalib-629> and <https://www.mdpi.com/article/10.3390/geosciences12010035/s1>, Table S1: Pn2MEET\_KSchulz: petrophysical and petrological characterisation of outcrop analogue samples before and after acidification; Table S2: Fluid Chemistry-AAS\_IC\_Photometry: chemical characterisation of spent acids after autoclave experiments, Table S3: Core Flooding Tests: permeability tracking during Core Flooding Tests.

**Author Contributions:** Conceptualisation, K.B. and K.E.S.; methodology, K.E.S.; validation, K.B. and K.E.S.; writing—original draft preparation, K.E.S.; writing—draft review, K.B., I.S.; visualisation, K.E.S.; supervision, K.B., I.S.; project administration, K.B.; funding acquisition, K.B., I.S. All authors have read and agreed to the published version of the manuscript.

**Funding:** The work is conducted as part of the MEET project that has received funding from the European Union's Horizon 2020 research and innovation programme under grant agreement No 792037.

**Institutional Review Board Statement:** Not applicable.

**Informed Consent Statement:** Not applicable.

**Data Availability Statement:** Supplementary Materials are published by Schulz et al. [42] and can be found at <https://doi.org/10.48328/tudatalib-629> (access date: 25 November 2021).

**Acknowledgments:** The present work was elaborated at the Institute of Applied Geosciences, Technical University of Darmstadt in the framework of the projects MEET (grant agreement No. 792037) and UDDGP. We would like to thank the supporting staff from the Department of Geothermal Science and Technology, namely G. Schubert, S. Schmidt, R. Seehaus, D. Scheuvsens and R. Petschik from Goethe University of Frankfurt for the XRD measurements, as well as our project partners related to MEET/UDDGP, to mention A. Genter, A. Turan, J. Reinecker, J. Gutmanis, R. Shail, B. Simons, C. Dalby. We would also like to acknowledge the editorial support of Mayes Nie and Aleksandar Pavlovic, as well as two anonymous reviewers, who allowed us to substantially improve our manuscript.

**Conflicts of Interest:** The authors declare no conflict of interest.

## Appendix A

Calculation of permeability from the measured pressure difference before and after the CFTs: the differential pressure and the runtime, which—under constant flow rate—can be expressed as multiples of the pore volume, are measured automatically during the CFTs. The evaluation of the measured pressure difference (given in psi) is based on Darcy's law. An additional multiplication factor, which depends on the device and on the conversion from bar (or Pa) to psi (1 bar = 14,504 psi), is used to calculate the permeability (OFITE, 2019). With  $k$ : permeability (mD);  $\mu$ : viscosity of fluid (cP);  $Q$ : flow rate (cm<sup>3</sup>/s);  $l$ : core length (cm);  $A$ : cross sectional area of the core (cm<sup>2</sup>);  $\Delta p$ : differential pressure (psi), the resulting equation is:

$$k = 14,700 \cdot \mu \cdot Q \cdot l / (A \cdot \Delta p) \quad (A1)$$

As described in Section 3.2, the permeability can only be measured during the pre- and post-flush. Since the viscosity of the brine (NH<sub>4</sub>Cl) is temperature dependent, it had

to be determined in additional experiments, conducted by Fangmann Energy Services. Nevertheless, to our knowledge, in the data provided by Fangmann Energy Services, which are included in the Supplementary Materials, the viscosity of the fluid was set to 1 cP.

To avoid falsification of the results, our evaluation of the CFTs is based on the PEF, which is introduced in Section 3.2 and allows a relative quantification of the permeability increase. The permeability changes were verified by additional gas permeability measurements, as described in Section 3.3.

The viscosity of the acids, considering the chemical reactions of the acids and under the applied temperatures, is unknown. Therefore, the tracking of the differential pressure—which is inversely proportional to the permeability—during the CFTs, as discussed in Section 3.2, is only a qualitative approach to the permeability changes during the CFTs.

## Appendix B

	Powder HCl+HF						Powder HCl	Plug HCl						Plug HCl+HF						CFT		
	1	2	3	4	5	6	3	1	2	3	4	5	6	1	2	3	4	5	6	3	5	6
Quartz	↑	↑	↑	↑	↑	↑	↑	↑	↑	↑	↑	↑	↑	↓	↑	o	o	↓	↓	↓	o	o
K-Feldspar	↓	↓	↓	↓	o	↓	↑	↓	↓	↑	↓	o	o	↓	↓	↑	↓	o	o	↓	↓	↓
Plagioclase	↓	↓	↓	o	↓	↓	o	↑	↑	↑	↑	o	o	↑	↓	o	↑	o	↑	↑	o	↑
Muscovite	↓	↓	↓	↓	↓	↓	↓	↓	↓	↓	↓	o	o	↓	↓	↓	↓	o	↑	o	o	↑
Biotite	o	o	o	o	↓	↓	o	o	o	o	o	↓	↓	o	o	o	o	↓	↓	o	↓	↓
Chlorite	o	o	o	o	o	↓	↓	o	o	o	o	o	↓	o	o	o	o	o	↓	o	↓	↓
Schörl	↓	↓	↓	↓	↓	↓	↓	o	↑	↑	↑	o	o	↑	o	o	↑	o	↑	↑	o	↑
Cassiterite	o	o	o	o	o	↑	o	o	o	o	o	o	o	o	o	o	o	o	o	o	o	o
Hieratite	o	↑	↑	↑	o	o	o	o	o	o	o	o	o	o	o	o	o	o	o	o	o	o

relative increase (↑), decrease (↓) or no significant changes (variation < 0,3 %) (o) after acidification

**Figure A1.** Comparison of the relative mineralogical composition before and after chemical treatment in AEs and CFTs.

## References

- Law, R.; Cotton, L.; Ledingham, P. The United Downs Deep Geothermal Power Project. In Proceedings of the European Geothermal Congress, Den Haag, The Netherlands, 11–14 June 2019.
- Beamish, D.; Busby, J. The Cornubian geothermal province: Heat production and flow in SW England: Estimates from boreholes and airborne gamma-ray measurements. *Geotherm. Energy* **2016**, *4*, 1–25. [\[CrossRef\]](#)
- Staněk, M.; Géraud, Y. Granite microporosity changes due to fracturing and alteration: Secondary mineral phases as proxies for porosity and permeability estimation. *Solid Earth* **2019**, *10*, 251–274. [\[CrossRef\]](#)
- Gleeson, S.A.; Wilkinson, J.J.; Stuart, F.M.; Banks, D.A. The Origin and Evolution of Base Metal Mineralising Brines and Hydrothermal Fluids, South Cornwall, UK. *Geochim. Cosmochim. Acta* **2001**, *65*, 2067–2079. [\[CrossRef\]](#)
- Simons, B.; Shail, R.K.; Andersen, J.C.Ø. The petrogenesis of the Early Permian Variscan granites of the Cornubian Batholith: Lower plate post-collisional peraluminous magmatism in the Rhenohercynian Zone of SW England. *Lithos* **2016**, *260*, 76–94. [\[CrossRef\]](#)
- Shail, R.K.; Leveridge, B.E. The Rhenohercynian passive margin of SW England: Development, inversion and extensional reactivation. *Comptes Rendus Geosci.* **2009**, *341*, 140–155. [\[CrossRef\]](#)
- Bromley, A. (Ed.) *Water-Rock Interaction in Southwest England: The Evolution of the Cornubian Orefield*; International Association of Geochemistry and Cosmochemistry: Lawrence, KS, USA, 1989; 58p.
- Willis-Richards, J. Three-dimensional modelling from gravity of the Carnmenellis granite pluton, West Cornwall. Paper presented at the Tenth UK Geophysical Assembly. *Geophys. J. Int.* **1986**, *92*, 323–334.
- Edmunds, W.M.; Kay, R.L.F.; McCartney, R.A. Origin of Saline Groundwaters in the Carnmenellis Granite (Cornwall, England): Natural Processes and Reaction during Hot Dry Rock Reservoir Circulation. *Chem. Geol.* **1985**, *49*, 287–301. [\[CrossRef\]](#)

10. Yeomans, C.; Middleton, M.; Shail, R.; Grebby, S.; Lusty, P. Regional Lineament Detection Using Bottom-Up Object-Based Image Analysis Methods. In Proceedings of the 80th EAGE Conference and Exhibition 2018, Copenhagen, Denmark, 11–14 June 2018; EAGE Publications BV: Houten, The Netherlands, 2018.
11. Yeomans, C.M.; Middleton, M.; Shail, R.K.; Grebby, S.; Lusty, P.A.J. Integrated Object-Based Image Analysis for semi-automated geological lineament detection in southwest England. *Comput. Geosci.* **2019**, *123*, 137–148. [[CrossRef](#)]
12. Ghosh, P.K. The Carnmenellis Granite: Its Petrology, Metamorphism and Tectonics. *Q. J. Geol. Soc.* **1934**, *90*, 240–276. [[CrossRef](#)]
13. Shail, R.K.; Alexander, A.C. Late Carboniferous to Triassic reactivation of Variscan basement in the western English Channel: Evidence from onshore exposures in south Cornwall. *J. Geol. Soc.* **1997**, *154*, 163–168. [[CrossRef](#)]
14. British Geological Survey. BGS Geology 625k | DiGMapGB-625: Digital Geology Data. BGS. 2007. Available online: <https://www.bgs.ac.uk/datasets/bgs-geology-625k-digmapgb/> (accessed on 25 November 2021).
15. Manning, D.A.C.; Hill, P.I.; Howe, J.H. Primary Lithological Variation in the Kaolinized St Austell Granite, Cornwall, England. *J. Geol. Soc.* **1996**, *153*, 827–838. [[CrossRef](#)]
16. Psyrillos, A.; Manning, D.; Burley, S. Geochemical constraints on kaolinization in the St Austell Granite, Cornwall, England. *J. Geol. Soc.* **1998**, *155*, 829–840. [[CrossRef](#)]
17. Tierney, R.L.; Glass, H.J. Modelling the structural controls of primary kaolinite formation. *Geomorphology* **2016**, *268*, 48–53. [[CrossRef](#)]
18. Zotov, A.; Mukhamet-Galeev, A.; Schott, J. An experimental study of kaolinite and dickite relative stability at 150–300 °C and the thermodynamic properties of dickite. *Am. Mineral.* **1998**, *83*, 516–524. [[CrossRef](#)]
19. Sanderson, D.J.; Roberts, S.; Gumiel, P.; Greenfield, C. Quantitative Analysis of Tin- and Tungsten-Bearing Sheeted Vein Systems. *Econ. Geol.* **2008**, *103*, 1043–1056. [[CrossRef](#)]
20. Geothermal Energy Limited. United Downs Deep Geothermal Power Project—Confidential Geology Summary Report. In Proceedings of the Redruth, 44th Workshop on Geothermal Reservoir Engineering Stanford University, Stanford, CA, USA, 11–13 February 2019.
21. Scrivener, C.; Darbyshire, D.P.; Shepherd, T. Timing and significance of crosscourse mineralization in SW England. *J. Geol. Soc.* **1994**, *151*, 587–590. [[CrossRef](#)]
22. Reinecker, J.; Gutmanis, J.; Cotton, L.; Foxford, A.; Dalby, C.; Law, R. Geothermal Exploration and Reservoir Modelling of the United Downs Deep Geothermal Project, Cornwall (UK). *Geothermics* **2021**, *97*, 102226. [[CrossRef](#)]
23. Bär, K.; Arbarim, R.; Turan, A.; Schulz, K.; Mahmoodpour, S.; Leiss, B.; Wagner, B.; Sosa, G.; Ford, K.; Trullenque, G.; et al. *Database of Petrophysical and Fluid Properties and Recommendations for Model Parametrization of the Four Variscan Reservoir Types*; MEET Report, Deliverable D5.5; Technical University of Darmstadt: Darmstadt, Germany, 2020; 110p.
24. Recalde Lummer, N.; Rauf, O. Premium Treatment System for Granite and Sandstone Formations: Fluid Development and Field Trial in a Geothermal Well. In Proceedings of the European Geothermal Congress, Den Haag, The Netherlands, 11–14 June 2019.
25. Ferreiro Mählmann, R.; Frey, M. Standardisation, Calibration and Correlation of the Kübler-Index and the Vitrinite/Bituminite Reflectance: An Inter-Laboratory and Field Related Study. *Swiss J. Geosci.* **2012**, *105*, 153–170. [[CrossRef](#)]
26. Micromeritics. Product Showcase AccuPyc II 1340: Specification Sheet. Available online: <https://www.micromeritics.com/Product-Showcase/AccuPyc-II-1340.aspx> (accessed on 12 November 2019).
27. Weydt, L.M.; Heldmann, C.-D.J.; Machel, H.G.; Sass, I. From oil field to geothermal reservoir: Assessment for geothermal utilization of two regionally extensive Devonian carbonate aquifers in Alberta, Canada. *Solid Earth* **2018**, *9*, 953–983. [[CrossRef](#)]
28. Weinert, S.; Bär, K.; Sass, I. Thermophysical rock properties of the crystalline Gonghe Basin Complex (Northeastern Qinghai-Tibet-Plateau, China) basement rocks. *Environ. Earth Sci.* **2020**, *79*, 77. [[CrossRef](#)]
29. Mielke, P.; Weinert, S.; Bignall, G.; Sass, I. Thermo-physical rock properties of greywacke basement rock and intrusive lavas from the Taupo Volcanic Zone, New Zealand. *J. Volcanol. Geotherm. Res.* **2016**, *324*, 179–189. [[CrossRef](#)]
30. Popov, Y.; Lippmann, E.; Rauen, A. TCS-Manual: TCS Thermal Conductivity (TC) and Thermal Diffusivity (TD) Scanner. Version 9.3.2020. Available online: [www.geophysik-dr-rauen.de/tcscan/technical\\_data.html](http://www.geophysik-dr-rauen.de/tcscan/technical_data.html) (accessed on 9 March 2020).
31. Filomena, C.M.; Hornung, J.; Stollhofen, H. Assessing Accuracy of Gas-Driven Permeability Measurements: A Comparative Study of Diverse Hassler-Cell and Probe Permeameter Devices. *Solid Earth* **2014**, *5*, 1–11. [[CrossRef](#)]
32. Van Leong, H.; Ben Mahmud, H. A preliminary screening and characterization of suitable acids for sandstone matrix acidizing technique: A comprehensive review. *J. Pet. Explor. Prod. Technol.* **2019**, *9*, 753–778. [[CrossRef](#)]
33. Bauer, M.; Freeden, W.; Jacobi, H.; Neu, T. (Eds.) *Handbuch Tiefe Geothermie: Prospektion, Exploration, Realisierung, Nutzung*; Springer: Berlin/Heidelberg, Germany, 2014; 867p.
34. BGRCI, BGHM. GisChem, BG Gefahrstoffinformationssystem Chemikalien: Datenblatt Fluorwasserstoffsäure ab 1% bis unter 7%. 2020. Available online: [https://www.gischem.de/download/01\\_0-007664-39-3-000400\\_5\\_1\\_2510.PDF](https://www.gischem.de/download/01_0-007664-39-3-000400_5_1_2510.PDF) (accessed on 13 August 2021).
35. Broekaert, J.A. *Analytical Atomic Spectrometry with Flames and Plasmas*; John Wiley & Sons: Hoboken, NJ, USA, 2006.
36. Skoog, D.A.; Leary, J.J. *Instrumentelle Analytik: Grundlagen, Geräte, Anwendungen*, 1st ed.; Springer: Berlin/Heidelberg, Germany, 1996.
37. Welz, B.; Sperling, M. *Atomabsorptionsspektrometrie*; Wiley-VCH: Weinheim, Germany, 1997.
38. Deutsches Institut für Normung e.V. *Deutsche Einheitsverfahren zur Wasser-, Abwasser- und Schlammuntersuchung; Anionen (Gruppe D); Photometrische Bestimmung von Gelöster Kieselsäure (D 21)*; Beuth Verlag GmbH: Berlin, Germany, 1990.

39. Petschick, R. MacDiff. 2017. Available online: <http://www.geol-pal.uni-frankfurt.de/Staff/Homepages/Petschick/classicsoftware.html> (accessed on 13 August 2021).
40. Petschick, R. Röntgendiffraktometrie in der Sedimentologie. Schriftenreihe der DGG. *Sediment* **2002**, *18*, 99–118.
41. Bruker AXS GMBH. *S8 Tiger—Introductory User Manual*; Bruker AXS GmbH: Karlsruhe, Germany, 2010.
42. Schulz, K.; Bär, K.; Sass, I. Petrophysical and Hydrochemical Dataset of Lab-Scale Permeability Enhancement Tests by Chemical Treatment in Fractured Granite (Cornubian Batholith, Cornwall, UK). 2021. Available online: <https://tudatalib.ulb.tu-darmstadt.de/handle/tudatalib/2925> (accessed on 25 November 2021). [[CrossRef](#)]
43. Kretz, R. Symbols for rock-forming minerals. *Am. Mineral.* **1983**, *68*, 277–279.
44. Fangmann Energy Services. *Permeability Tests with Granite Cores under Borehole Conditions. Lab Report 19-033 for Institute of Applied Geosciences*; Technical University of Darmstadt: Darmstadt, Germany, 2019.
45. Lever, A.B. *Inorganic Electronic Spectroscopy*; Wiley: Amsterdam, The Netherlands, 1983.
46. Portier, S.; Vuataz, F.D. Developing the ability to model acid-rock interactions and mineral dissolution during the RMA stimulation test performed at the Soultz-sous-Forêts EGS site, France. *Comptes Rendus Geosci.* **2010**, *342*, 668–675. [[CrossRef](#)]
47. Portier, S.; André, L.; Vuataz, F.D. *Review on Chemical Stimulation Techniques in Oil Industry and Applications to Geothermal Systems: Deep Heat Mining Association, Engine, Work Package 4*; Technical Report; DHM: Neuchâtel, Switzerland, 2007; 34p.
48. Economides, M.J.; Nolte, K.G. *Reservoir Stimulation*; Prentice Hall: Englewood Cliffs, NJ, USA, 1989; Volume 2.
49. Sclar, C.B.; Fahey, J.J. The staining mechanism of potassium feldspar and the origin of hieratite. *Am. Mineral.* **1972**, *57*, 287–291.
50. Tariq, Z.; Mahmoud, M.; Abdulraheem, A.; Al-Nakhli, A.; Bataweel, M. A review of pulse fracturing treatment: An emerging stimulation technique for unconventional reservoirs. In Proceedings of the SPE Middle East Oil and Gas Show and Conference, Manama, Bahrain, 15 March 2019. [[CrossRef](#)]
51. Tariq, Z.; Aljawad, M.S.; Mahmoud, M.; Abdulraheem, A.; Al-Nakhli, A.R. Thermochemical acid fracturing of tight and unconventional rocks: Experimental and modeling investigations. *J. Nat. Gas Sci. Eng.* **2020**, *83*, 103606. [[CrossRef](#)]
52. Baujard, C.; Genter, A.; Dalmais, E.; Maurer, V.; Hehn, R.; Rosillette, R.; Vidal, J.; Schmittbuhl, J. Hydrothermal characterization of wells GRT-1 and GRT-2 in Rittershoffen, France: Implications on the understanding of natural flow systems in the rhine graben. *Geothermics* **2017**, *65*, 255–268. [[CrossRef](#)]
53. Nami, P.; Schellschmidt, R.; Schindler, M.; Tischner, T. Chemical Stimulation Operations for Reservoir Development of the Deep Crystalline HDR/EGS System at Soultz-Sous-Forêts (France). In Proceedings of the 32nd Workshop on Geothermal Reservoir Engineering, Stanford, CA, USA, 22–24 January 2008; pp. 28–30.
54. Schill, E.; Genter, A.; Cuenot, N.; Kohl, T. Hydraulic performance history at the Soultz EGS reservoirs from stimulation and long-term circulation tests. *Geothermics* **2017**, *70*, 110–124. [[CrossRef](#)]